RSC Advances

PAPER

View Article Online
View Journal | View Issue

Check for updates

Cite this: *RSC Adv.*, 2022, **12**, 5910

High-performance quasi-solid-state flexible supercapacitors based on a flower-like NiCo metal–organic framework†

Yongquan Du,‡[a] Ruibin Liang,‡[a] Junxi Wu,[a] Yingyi Ye,[a] Shaoyong Chen,[a] Jian Yuan,[a] Jianwen Chen[c] and Peng Xiao*[ab]

Received 2nd December 2021
Accepted 10th February 2022

DOI: 10.1039/d1ra08785a

rsc.li/rsc-advances

NiCo metal–organic framework (MOF) electrodes were prepared by a simple hydrothermal method. The flower-like NiCo MOF electrode exhibited an exciting potential window of 1.2 V and an excellent specific capacitance of 927.1 F g^{-1} at 1 A g^{-1}. The flower-like NiCo MOF//activated carbon (AC) device delivered a high energy density of 28.5 W hkg^{-1} at a power density of 400.5 W kg^{-1} and good cycle stability (95.4% after 5000 cycles at 10 A g^{-1}). Based on the flower-like NiCo MOF electrode, the asymmetric quasi-solid-state flexible supercapacitor (AFSC) was prepared and exhibited good capacitance retention after bending (79% after 100 bends and 64.4% after 200 bends). Furthermore, two AFSCs in series successfully lit up ten parallel red LED lights, showing great application potential in flexible and wearable energy storage devices.

1. Introduction

As the energy crisis continues to intensify, green and efficient energy storage devices have attracted more and more attention. Among many energy devices, supercapacitors have become the subject of much attention due to the advantages of high power density, fast charge and discharge, and long cycle life.[1,2] As the key part of supercapacitors, electrode materials play an important role in the performance of supercapacitors.[3,4] The electrode materials can be divided into two types: carbon materials and pseudocapacitive materials.[5,6] Carbon materials only involve physical adsorption and desorption during the charging and discharging process, which is helpful for high stability and long cycle life.[7,8] For pseudocapacitive materials, reversible redox reactions will happen during the charging and discharging process, which is helpful for high specific capacitance.[9,10] Increasing the specific surface area and pseudocapacitance are beneficial to improve the specific capacitance.[11–13] The specific capacitance is one of the key factors affecting the energy density of supercapacitors.[14,15] In addition, the assembly process of the supercapacitors also has a great impact on the energy density.[16,17] Especially for flexible supercapacitors, high stable electrochemical performance needs to be ensured by good mechanical performance.[18,19] Therefore, the assembly process of supercapacitors plays an important role in obtaining high energy density.

Metal–organic frameworks (MOFs) are a new type of material composed of metal ions and organic ligands,[20,21] which have the advantages of both redox sites and a large theoretical specific surface area (46 000 m^2 g^{-1}).[22] However, the most of MOFs with inherent low conductivity limit the application in supercapacitors.[23–25] In order to improve conductivity of MOFs, the preparation of different structures and combinations of MOFs becomes one of the current research directions.[26–28] Many studies have showed that MOFs with a unique structure exhibit a large specific surface area, reducing the diffusion distance of electrolyte ions, thus achieving an increase in conductivity.[29,30] For example, NiCo MOF with polycrystalline structure prepared by Ye *et al.*[31] exhibited a high specific capacity of 833 C g^{-1} at 0.5 A g^{-1} and maintained 714 C g^{-1} at 20 A g^{-1}. The uniform substitution of Co^{2+} for Ni^{2+} in MOFs increased the free holes, resulting in good conductivity and polycrystalline structure buffered the volume change during charge–discharge process, resulting in excellent capacitance retention rate. The accordion-like Ni MOF had specific surface area of 117.42 m^2 g^{-1} and average pore size of 5 nm, which was conducive to enhancing the diffusion of ions and electrolytes and improved electrochemical performance.[32] Xu *et al.*[33] used a room temperature solution phase method to synthesize low-crystalline Ni/Co MOF with extraordinary charge storage capabilities. This can be attributed to its disordered structure and small nanosheet feature size (<100 nm) to increase the specific surface area.

[a]*School of Physics and Optoelectronic Engineering, Foshan University, Foshan 528000, China. E-mail: xiaopeng@fosu.edu.cn*

[b]*Guangdong–Hong Kong–Macao Joint Laboratory for Intelligent Micro–Nano Optoelectronic Technology, Foshan 528000, China*

[c]*School of Electronic and Information Engineering, Foshan University, Foshan 528000, China*

† Electronic supplementary information (ESI) available. See DOI: 10.1039/d1ra08785a

‡ These authors contributed equally to this work.

Open Access Article. Published on 16 February 2022. Downloaded on 12/9/2025 1:56:21 AM. This article is licensed under a Creative Commons Attribution-NonCommercial 3.0 Unported Licence.

© 2022 The Author(s). Published by the Royal Society of Chemistry

Open Access Article. Published on 16 February 2022. Downloaded on 12/9/2025 1:56:21 AM.
This article is licensed under a Creative Commons Attribution-NonCommercial 3.0 Unported Licence.

Significantly, the structure and size of nanosheet are very important for improving conductivity of MOFs. This is because the special nanosheet structure can reduces the ion diffusion distance and increases the specific surface area by reducing the size of the material particles to the nanoscale.[32,34,35] Therefore, it is very necessary to study to control the size and structure of the nanosheets of MOFs.

Herein, we used a simple hydrothermal method to synthesize NiCo MOF-x ($x = 0, 2, 4$), where x represented the volume of 0.8 M NaOH. In particular, NiCo MOF-2 exhibited a large potential window of 1.2 V and a specific capacitance of 927.1 F g^{-1} at 1 A g^{-1}. With NiCo MOF-2 as the positive electrode and activated carbon (AC) as the negative electrode, the assembled aqueous device delivered a superior energy density of 28.5 W h kg^{-1} at a power density of 400.5 W kg^{-1} and amazing cycle stability (95.4% capacitance retention after 5000 cycles). Furthermore, the asymmetric flexible quasi-solid-state supercapacitor (AFSC) was assembled and demonstrated the energy density of 20.4 W h kg^{-1} at the power density of 901.5 W kg^{-1}. Finally, two AFSCs in series successfully lit up ten parallel red LED lights and exhibited surprising capacitance retention rate after bending (79% after 100 bends and 64.4% after 200 bends), showing the huge potential in flexible electronics.

2. Experiment section

2.1 Chemicals

Cobalt chloride hexahydrate (MW = 237.93, $CoCl_2 \cdot 6H_2O$), nickel chloride hexahydrate (MW = 237.7, $NiCl_2 \cdot 6H_2O$), polyvinyl alcohol (PVA, MW = 44), dimethylformamide (DMF, MW = 73.09, $HCON(CH_3)_2$) and activated carbon (AC) were purchased from Macklin. Terephthalic acid (PTA, MW = 166.13, $C_8H_6O_4$), sodium hydroxide (MW = 40.01, NaOH) were purchased from Jiuding Chemical. NaOH solution was prepared with deionized water, and other solutions were prepared with DMF.

2.2 Preparation of NiCo MOF samples

NiCo MOF samples were prepared by a simple hydrothermal method. Firstly, 30 mL of DMF was added to a 100 mL beaker, and then 0.332 g of PTA was added and sonicated for 30 min. Secondly, 0.156 g $NiCl_2 \cdot 6H_2O$ and 0.157 g $CoCl_2 \cdot 6H_2O$ were added, and stirred at room temperature for 30 min. During the stirring process, the NaOH solution was added and ultrasonicated for 30 min. Then, the mixed solution was poured into a 100 mL high-temperature reaction kettle at 100 °C for 10 h. NiCo MOF samples were washed with DMF and alcohol for two times after cooling down naturally. Finally, NiCo MOF samples were put into a vacuum box and dried at 60 °C for 12 h. The addition of 0.8 M NaOH solution was 0 mL, 2 mL and 4 mL and they were represented by NiCo MOF-x ($x = 0, 2, 4$).

2.3 Preparation of NiCo MOF-x electrode and AC electrode

NiCo MOF-x electrode were prepared by slurry coating technology. Firstly, NiCo MOF-x powder, acetylene black and polyvinylidene fluoride (PVDF) with a weight ratio of 8 : 1 : 1 were formed a suspension in DMF solvent. Then, the slurries were coated on Ni foam with an area of 1×1 cm^2. Finally, two pieces of Ni foam with slurry in the middle were pressed under a pressure of 8 MPa. The weight loading of NiCo MOF-x on the Ni foam was about 4 mg.

The preparation process of AC electrode was the same as NiCo MOF-x electrode.

2.4 Preparation of KOH/PVA gel electrolyte

Firstly, 3 g PVA was added to 30 mL deionized water. Then the solution was stirred at 85 °C until clear. After that, 10 mL 3 M KOH solution was added to the above solution, stirring evenly to obtain KOH/PVA gel electrolyte.

2.5 Preparation of asymmetric supercapacitor

2.5.1 Preparation of asymmetric aqueous supercapacitor. With NiCo MOF-2 electrode as positive electrode, AC electrode as negative electrode, the asymmetric aqueous supercapacitor was test in 3 M KOH aqueous electrolyte.

2.5.2 Preparation of asymmetric quasi-solid-state supercapacitor (ASC). The ASC in a sandwich structure was assembled by NiCo MOF-2 electrode as positive electrode, AC electrode as negative electrode and KOH/PVA as gel electrolyte.

2.5.3 Preparation of asymmetric quasi-solid-state flexible supercapacitor (AFSC). Firstly, Ni foam pressed by 2 MPa were used as the flexible substrate to prepare the NiCo MOF-2 electrode and AC electrode. The assembly process of AFSC was the same as ASC.

2.6 Characterization

X-ray diffraction (XRD, Smartlab 9 kW) patterns of NiCo MOF samples are obtained in the Bragg's angle (2θ) range from 10° to 50° with monochromatic Cu Kα radiation. X-ray photoelectron spectroscopy (XPS, Nexsa) measurements are performed to analyze the surface species and their chemical states. A field emission scanning electron microscopy (FE-SEM, HITACHI SU8200) combined with energy dispersive X-ray spectroscopy (EDS) are used to analyze the morphology and element distribution of samples. The specific surface area of samples are investigated by the Brunauer–Emmett–Teller (BET) method (ASAP2020).

2.7 Electrochemical measurement

The electrochemical performance test is carried out in the three-electrode system of the electrochemical workstation (CompactStat.h). The prepared electrode, platinum electrode and saturated calomel electrode are used as working electrode, auxiliary electrode and reference electrode, respectively. In 3 M KOH aqueous solution, cyclic voltammetry (CV), constant current charge and discharge (GCD) and electrochemical impedance spectroscopy (EIS) measurements are performed at room temperature, and the potential window of CV and GCD is −0.4–0.8 V and 0–0.45 V, respectively. The specific capactance is generally calculated by the eqn (1).[36]

Open Access Article. Published on 16 February 2022. Downloaded on 12/9/2025 1:56:21 AM.
This article is licensed under a Creative Commons Attribution-NonCommercial 3.0 Unported Licence.

$$C = \frac{I\Delta t}{m\Delta V} \quad (1)$$

where C (F g^{-1}) is the mass specific capacitance, I (A) is the discharge current, Δt (s) is the discharge time, m (g) is the mass of the active material and ΔV (V) is the discharge voltage.

The preparation of supercapacitors firstly needs to ensure that the charges of the positive electrode and negative electrode are equal ($Q_+ = Q_-$). The optimal mass ratio between the positive electrode and negative electrode is obtained according to eqn (2) and (3).[11,12]

$$Q = C \times m \times \Delta V \quad (2)$$

$$\frac{m+}{m-} = \frac{C- \times \Delta V-}{C+ \times \Delta V+} \quad (3)$$

where Q is the electrode charges, m (g) is the mass of the active material and ΔV (V) is the discharge voltage.

The specific capacitance, energy density and power density of supercapacitors are generally calculated through the eqn (4)–(6).[13,14,19,20]

$$C_1 = \frac{I\Delta t}{MV} \quad (4)$$

$$E = \frac{1}{2} \times \frac{1}{3.6} \times C_1 V^2 \quad (5)$$

$$P = 3600 \times \frac{E}{\Delta t} \quad (6)$$

where C_1 (F g^{-1}) is the specific capacitance of the supercapacitor, V (V) is the potential window of the supercapacitor and M (g) is the total mass of the active material in the negative and positive electrode material. E (W h kg^{-1}) is the energy density and P (W kg^{-1}) is the power density.

3. Results and discussion

Fig. 1 is the preparation process of NiCo MOF-2 with a flower-like structure. First, Ni^{2+}/Co^{2+} with mole ration of 1 : 1 and 1 mM PTA were added to the DMF solution, sonicating for 30 min. Then 2 mL (0.8 M) NaOH solutions were added to the DMF solution, and stirred for 30 min. After that, the obtained blue mixed solution was put into a 100 mL reaction vessel and reacted at 100 °C for 10 hours. At last, the flower-like NiCo MOF-2 was obtained.

Fig. 2(a) is the XRD patterns of NiCo MOF samples obtained from different addition of NaOH. The similar XRD patterns of NiCo MOF-2 and NiCo MOF-4 indicated the addition of NaOH only changed the morphology, which had not caused a change in crystallinity. It could be seen that all the peaks of the NiCo MOF samples were well indexed to $C_8H_6NiO_5 \cdot H_2O$ (PDF # 35-1677). This could be explained interpreted that Co^{2+} partially replaced Ni^{2+} in the metal–organic framework, retaining the crystal structure of $C_8H_6NiO_5 \cdot H_2O$.[25,29,30]

Fig. 2(b) is the XPS survey spectrum of NiCo MOF-2, including four elements of Ni, Co, O, and C. As shown in Fig. 2(c), the satellite peaks of Ni $2p_{3/2}$ and Ni $2p_{1/2}$ were located at 863.7 and 882.3 eV, respectively, and the main peaks of Ni $2p_{3/2}$ and Ni $2p_{1/2}$ were 858.4 and 876.1 eV, with a spin-energy separation of 17.7 eV. The above results indicated that the Ni element in NiCo MOF-2 existed in the form of Ni^{2+}.[37,38] As shown in Fig. 2(d), the satellite peaks of Co $2p_{3/2}$ and Co $2p_{1/2}$ were located at 788.1 eV and 804.6 eV, respectively, and the main peaks of Co $2p_{3/2}$ and Co $2p_{1/2}$ were 783.5 eV and 799.3 eV, with a spin–energy separation of 15.8 eV, indicating that the Co element in NiCo MOF-2 existed in the form of Co^{2+}.[33,39] As shown in Fig. 2(e), the O 1s spectrum was deconvoluted into two peaks at 530.8 and 533 eV, which were associated with the C–O and metal–oxygen bonds M–O–M, respectively.[25,33] The C 1s spectrum (Fig. 2(f)) showed two peaks at 288.6 and 284.8 eV, which were associated with the O–C=O, C–C bonds of terephthalate, respectively.[31,37] The XPS results further confirmed the presence of nickel–cobalt terephthalate framework in the NiCo MOF-2.[32,37]

Fig. 3(a–d) show the SEM images of NiCo MOF samples. With the addition of NaOH, both NiCo MOF-2 and NiCo MOF-4 were formed by numerous nanosheets with good crystallinity. This could be explained that the NaOH affected the formation of nanosheets. In addition, NiCo MOF-2 and NiCo MOF-4 exhibited flower-like and layered structures, respectively, and we speculated that different alkaline conditions may affect the stacking pattern of nanosheets (shown in Fig. S1†). Various levels of stress and defects may play an important role in this morphology change.[33,35] The layered structure of NiCo MOF-4 was similar to the reported Ni MOF.[32] The formation

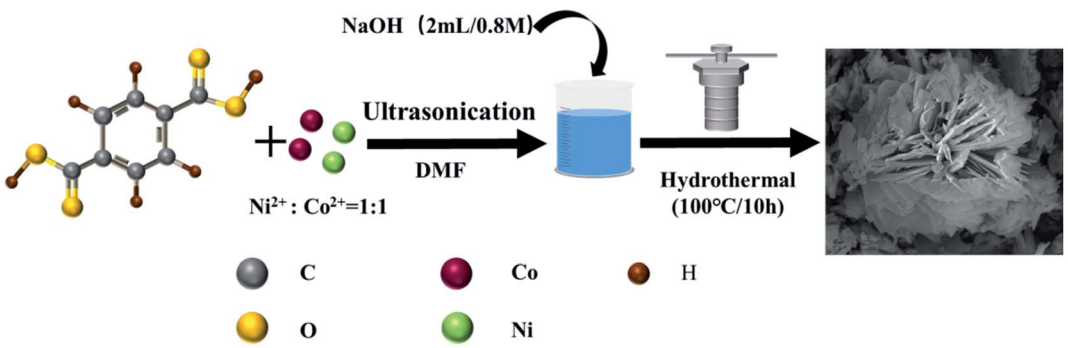

Fig. 1 Schematic illustration of the synthetic process of NiCo MOF-2.

© 2022 The Author(s). Published by the Royal Society of Chemistry

Open Access Article. Published on 16 February 2022. Downloaded on 12/9/2025 1:56:21 AM.
This article is licensed under a Creative Commons Attribution-NonCommercial 3.0 Unported Licence.

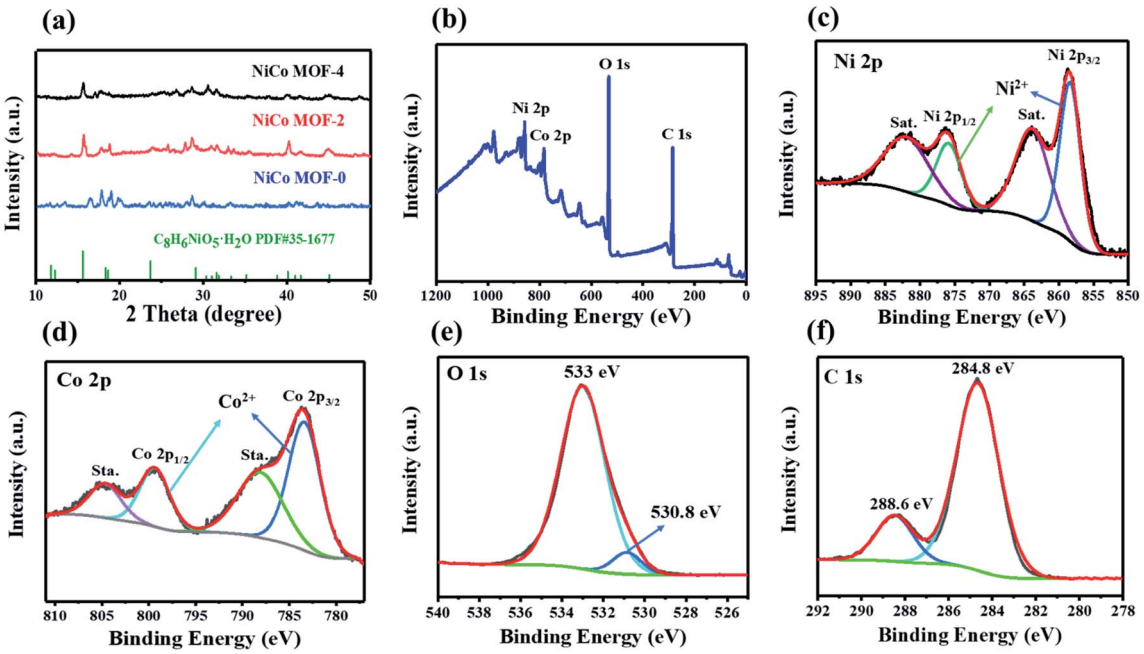

Fig. 2 (a) XRD patterns of NiCo MOF-0, NiCo MOF-2 and NiCo MOF-4. (b) XPS spectra of NiCo MOF-2. High-resolution of XPS spectra for Ni 2p (c), Co 2p (d), O 1s (e) and C 1s (f).

mechanism of the flower-like NiCo MOF-2 was still unclear, and further experimental and theoretical researches were needed. Fig. 3(e) is elemental mapping of NiCo MOF-2. The three elements of C, Co and Ni were well distributed in NiCo MOF-2, which also proved that Co^{2+} certain partially replaced Ni^{2+} in the metal–organic framework.

In Fig. 4(a and b) and Table 1, the specific surface area and pore size of NiCo MOF samples are characterized by BET measurement. The specific surface area of NiCo MOF-0, NiCo MOF-2 and NiCo MOF-4 were 5.83, 30.47 and 14.69 $m^2\ g^{-1}$, respectively. According to the Barrett–Joyner–Halenda (BJH) method, the average pore size of NiCo MOF-0, NiCo MOF-2 and NiCo MOF-4 were 26.55, 20, 23.89 nm, respectively. Obviously, the NiCo MOF-2 had the highest specific surface area. High specific surface area and stable pore size are beneficial to increase the number of redox sites and enhance ion transport efficiency in electrochemical reactions.[23,38,39]

In order to evaluate the electrochemical performance of NiCo MOFs, we conducted electrochemical tests in 3 M KOH aqueous electrolyte (shown in Fig. S2†). As shown in Fig. 5(a), the CV curves of NiCo MOF-2 were tested at different scan rates in the potential window of 1.2 V. NiCo MOF-2 had obvious redox peaks and exhibited good pseudo-capacitance behavior at the scan rate from 10 mV s^{-1} to 150 mV s^{-1}. This could be ascribed to the faradaic reaction between Ni^{2+}/Ni^{3+}, Co^{2+}/Co^{3+} and OH^-.[40] With the increase of the scanning rate, the shape of the

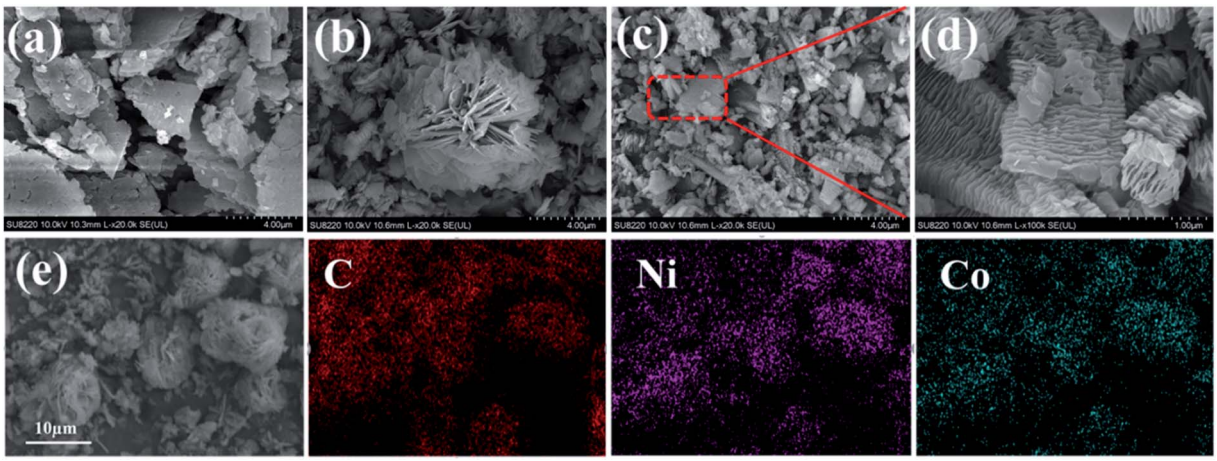

Fig. 3 SEM images of (a) NiCo MOF-0, (b) NiCo MOF-2, (c and d) NiCo MOF-4, (e) elemental mapping of NiCo MOF-2.

Open Access Article. Published on 16 February 2022. Downloaded on 12/9/2025 1:56:21 AM.
This article is licensed under a Creative Commons Attribution-NonCommercial 3.0 Unported Licence.

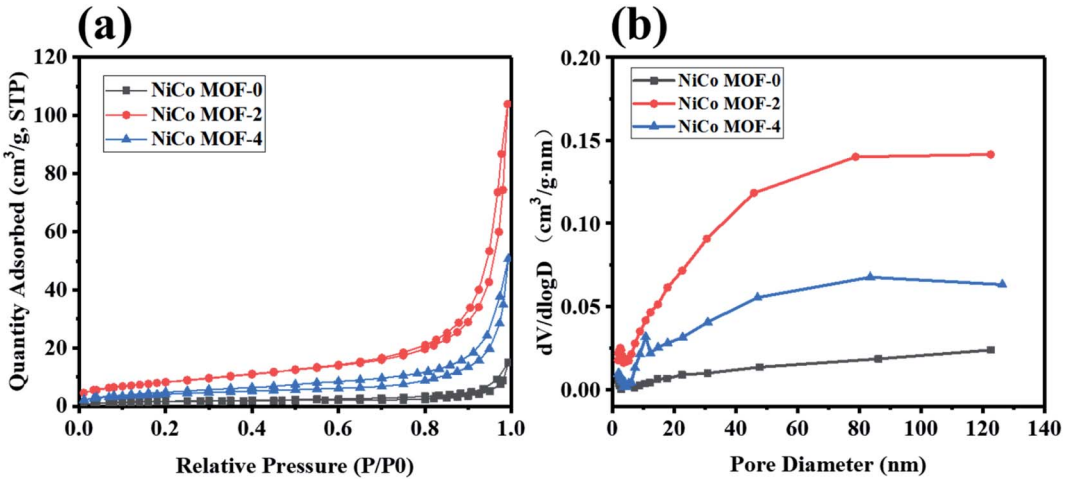

Fig. 4 (a) Specific surface area and (b) the pore size distribution of NiCo MOF samples.

Table 1 Specific surface area and average pore size of NiCo MOF samples

Samples	Specific surface area ($m^2\ g^{-1}$)	Average pore size (nm)
NiCo MOF-0	5.83	26.55
NiCo MOF-2	30.47	20
NiCo MOF-4	14.69	23.89

CV curve of NiCo MOF-2 remained basically unchanged, showing good magnification performance.[27] What's more, the positions of the oxidation peak and the reduction peak moved slightly to the positive and negative potential, which was mainly related to the internal resistance of the electrode materials.[41]

In Fig. 5(b), the specific capacitance of NiCo MOF-2 was 927.1, 873.3, 820.8, 769.5, 646.6 F g^{-1} at current densities of 1, 3, 5, 7 and 10 A g^{-1}. As shown in Table 2, the specific capacitance of NiCo MOF-2 in our work was higher than that reported in most of literature. In Fig. 5(c and d), NiCo MOF-2 had the

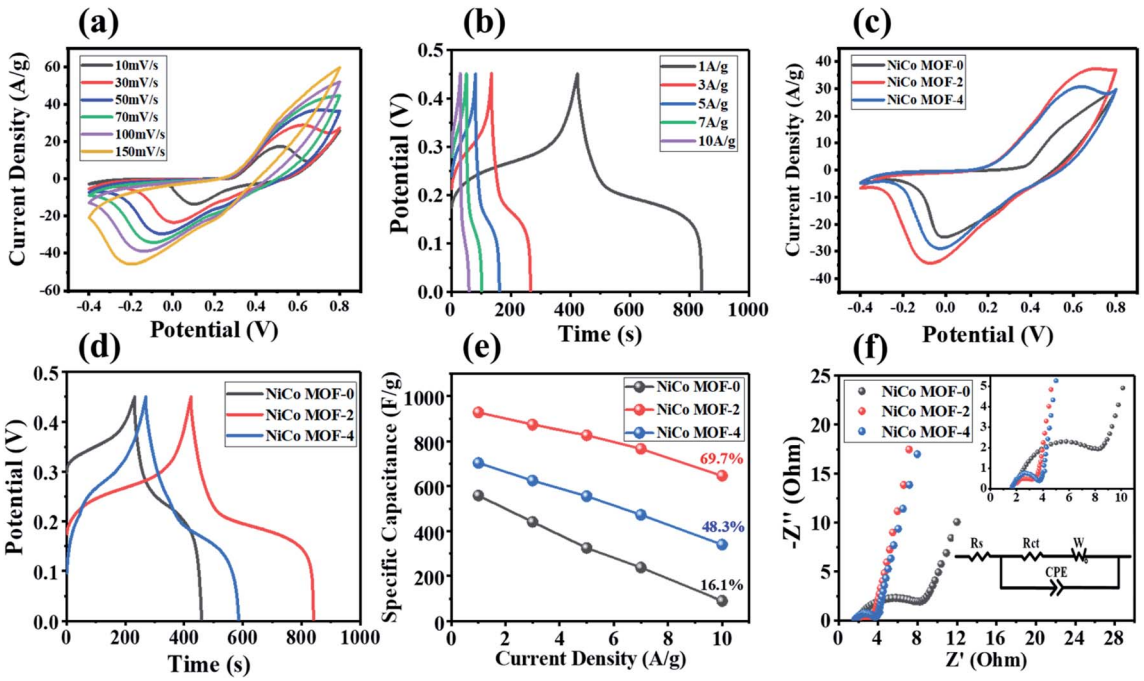

Fig. 5 Electrochemical performances of NiCo MOF-0, NiCo MOF-2 and NiCo MOF-4 in 3 M KOH solution. (a) CV curves at various scan rate from 10 to 150 mV s^{-1}, and (b) GCD curves at different current densities from 1 to 10 A g^{-1} of NiCo MOF-2. (c) CV curves at scan rate 50 mV s^{-1}, and (d) GCD curves at current densities 1 A g^{-1} of NiCo MOF-0, NiCo MOF-2, NiCo MOF-4, respectively. (e) The relationship between specific capacitance and current density (f) the Nyquist curves in the frequency range of 0.01 Hz to 100 kHz.

© 2022 The Author(s). Published by the Royal Society of Chemistry

Open Access Article. Published on 16 February 2022. Downloaded on 12/9/2025 1:56:21 AM.
This article is licensed under a Creative Commons Attribution-NonCommercial 3.0 Unported Licence.

Table 2 Specific capacitance values of MOF-based materials

Electrode materials	Electrolyte	Current density	Specific capacitance	Ref.
Fe-based MOF/GA	1 M TEA-BF_4/PC	20 A g^{-1}	353 F g^{-1}	26
Accordion-like Ni-MOF	3 M KOH	1.4 A g^{-1}	988 F g^{-1}	32
NiCo-MOF/AB	2 M KOH	0.5 A g^{-1}	916.1 F g^{-1}	37
Ni–CoP@C@CNT	3 M KOH	1 A g^{-1}	708.1 F g^{-1}	49
Co-MOF/D	3 M KOH	2 A g^{-1}	393.4 F g^{-1}	51
Co-MOF/E	3 M KOH	2 A g^{-1}	654.4 F g^{-1}	51
Co-MOF/W	3 M KOH	2 A g^{-1}	626.9 F g^{-1}	51
Ni-MOF	2 M KOH	1 A g^{-1}	726 F g^{-1}	54
MWCNTs@Ni-MOF	2 M KOH	2 A g^{-1}	890 F g^{-1}	55
Pillar Ni-MOF	2 M KOH	1 A g^{-1}	552 F g^{-1}	56
Flower-like NiCo MOF	**3 M KOH**	**1 A g^{-1}**	**927.1 F g^{-1}**	**This work**

longest discharge time and exhibited the largest specific capacitance. The flat charge–discharge potential plateau in Fig. 5(d) corresponding to the sharp redox peak in Fig. 5(c) further demonstrated the battery electrode characteristics of these NiCo MOF samples.[37] Fig. 5(e) summarized the capacitance retention rate of three NiCo MOF samples at different current densities. When the current density reached at 10 A g^{-1}, the capacitance retention rate of NiCo MOF-2, NiCo MOF-4 and NiCo MOF-0 were 69.7%, 48.3% and 16.1%, respectively. The high specific capacitance of NiCo MOF-2 electrode could be ascribed to the following reasons: (i) the good crystal phase of NiCo MOF-2 provides a high density of active sites to achieve large capacitance.[32,42] (ii) The ultrafine nanostructure further

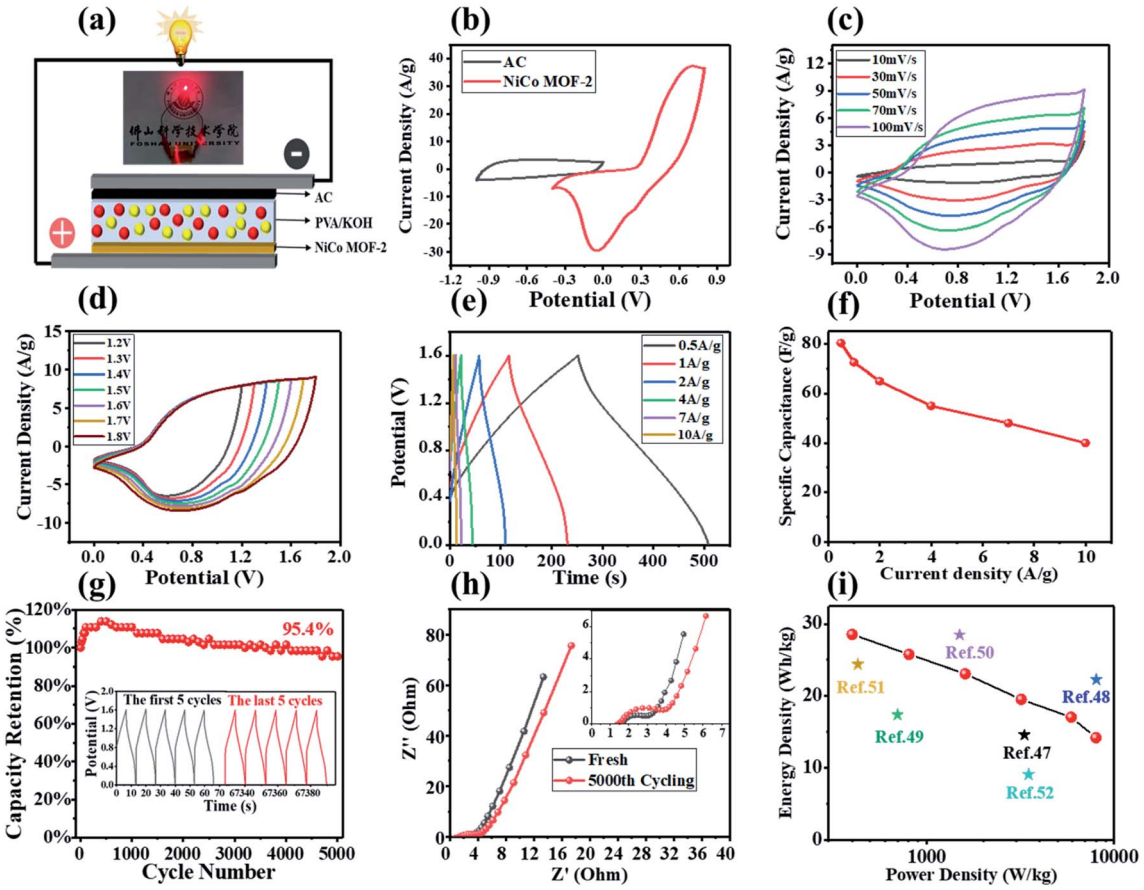

Fig. 6 (a) Schematic illustration of ASC and one red LED lights up by one ASC; with the NiCo MOF-2 positive electrode and the AC negative electrode in a three-electrode test: (b) CV curves at 40 mV s^{-1}; (c) comparison of CV curves at different scan rates; (d) CV curves in various potential windows at scan rate of 100 mV s^{-1}; (e) GCD curves at different current densities; (f) specific capacitance at different current densities; (e) GCD curves at different current densities; (g) cycling performance at a current density of 10 A g^{-1}; (h) Nyquist diagram before and after 5000 cycles; (i) Ragone plots compared to the reference.

Open Access Article. Published on 16 February 2022. Downloaded on 12/9/2025 1:56:21 AM.
This article is licensed under a Creative Commons Attribution-NonCommercial 3.0 Unported Licence.

presents large specific surface area, which is conducive to the short ion diffusion path of the rapid redox reaction.[33,43]

In Fig. 5(f), the intercept on the real axis and diameter of the semicircle of the EIS diagram represent the equivalent series resistance (R_s) and charge transfer resistance (R_{ct}) of the electrode, respectively.[22,28,31] According to fitting equivalent circuit analysis, the R_s of the NiCo MOF-0, NiCo MOF-2 and NiCo MOF-4 samples were 1.43, 1.61 and 1.75 Ω, respectively. The R_{ct} of the NiCo MOF-0, NiCo MOF-2 and NiCo MOF-4 samples were 2.80, 1.41 and 1.70 Ω, respectively. The R_{ct} of NiCo MOF-2 were the smallest, indicating that the efficiency of electron transfer was the highest. The slope of the straight line in the low frequency region represents the diffusion resistance of ions between the electrolyte and the electrode surface.[28,35] It showed that the NiCo MOF-2 exhibited the smallest diffusion resistance. These results further proved that NiCo MOF-2 had the best electrochemical performance in the three NiCo MOF samples.

Considering the practical application of NiCo MOF-2 electrode material, we assembled an ASC device of NiCo MOF-2//AC, and successfully lit up a red LED light in Fig. 6(a). As shown in Fig. 6(b), the potential window of the NiCo MOF-2//AC hybrid device could be extended to 1.8 V, and the effective mass ratio of NiCo MOF-2 and AC was 1 : 4 according to the eqn (3). The NiCo MOF-2//AC hybrid device was tested in a 3 M KOH aqueous electrolyte. The shape of the CV curves from 10 to 100 mV s^{-1} remained unchanging, showing good capacitance behavior in Fig. 6(c).[20] In addition, the NiCo MOF-2//AC hybrid device showed typical hybrid capacitance behavior, which was derived from the pseudocapacitance of the NiCo MOF-2 electrode and the double-layer capacitance of the AC electrode, respectively.[44] In the potential range from 1.2 to 1.8 V, CV curves were used to further study the potential window of the NiCo MOF-2//AC hybrid device at a scan rate of 100 mV s^{-1}. As shown in Fig. 6(d), no polarization phenomenon was observed in the CV curve, indicating the satisfactory capacitive behave.[45,46]

As shown in Fig. 6(e), the NiCo MOF-2//AC hybrid device had symmetric GCD curve at current densities of 0.5, 1, 2, 4, 7, 10 A g^{-1}, indicating its good cycle stability.[20] In Fig. 6(f), the specific capacitance of the NiCo MOF-2//AC hybrid device was 80.3 F g^{-1} at 0.5 A g^{-1}, and 40 F g^{-1} was remained at 10 A g^{-1}. The NiCo MOF-2//AC hybrid device had a capacitance retention rate of 95.4% after 5000 GCD tests (Fig. 6(g)). It was obvious that the specific capacitance first increased and then decreased during the GCD tests. The increase could be ascribed to the complete activation of the electrode and the decrease could be explained by the loss of electrode due to the continuous redox

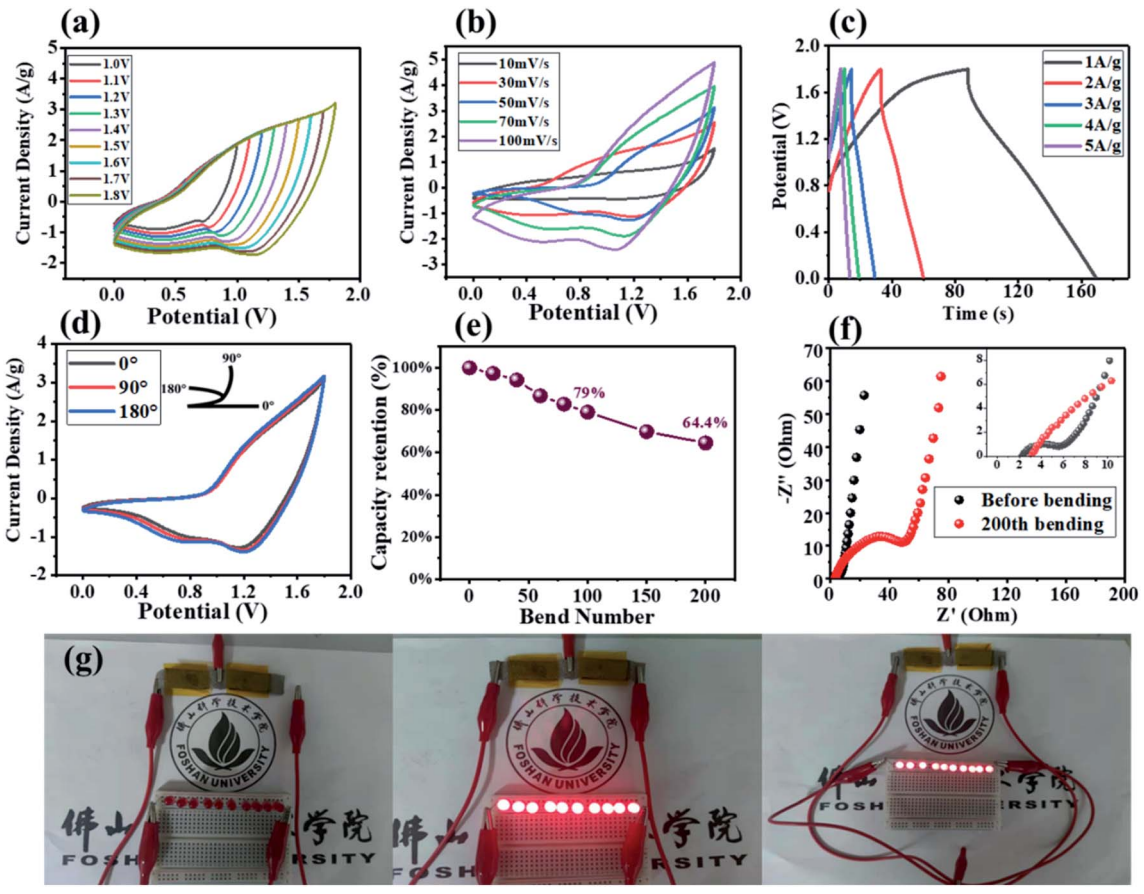

Fig. 7 (a) CV curves of AFSC in various potential windows at scan rate of 50 mV s^{-1}; (b) comparison of CV curves for AFSC at different scan rates; (c) GCD of ASC at different current densities; (d) CV curves of AFSC in different bending states at scan rate of 50 mV s^{-1}. (e) Capacitance retention of AFSC after repeated bending. (f) Nyquist diagram of the AFSC before and after 200 bending. (g) Two AFSC light up 10 red LED lights.

© 2022 The Author(s). Published by the Royal Society of Chemistry

Open Access Article. Published on 16 February 2022. Downloaded on 12/9/2025 1:56:21 AM.
This article is licensed under a Creative Commons Attribution-NonCommercial 3.0 Unported Licence.

reaction in the GCD test.[37,47] As shown in Fig. 6(h), the R_s changed from 1.53 Ω to 1.43 Ω, and R_{ct} slightly increased after 5000 GCD tests, indicating that the NiCo MOF-2//AC hybrid device met the requirements of high-performance supercapacitors.[48] As shown in Fig. 6(i), the maximum energy density of the NiCo MOF-2//AC hybrid device was 28.5 W h kg^{-1} at a power density of 400.5 W kg^{-1}. Even at a power density of 7998.7 W kg^{-1}, the energy density remained at 14.2 W h kg^{-1}, which were advantageous over many previously reported ASCs, such as Ni–CoP@C@CNT//AC (17.4 W h kg^{-1} at 699.1 W kg^{-1}),[49] CoNi-MOF//AC (28.5 W h kg^{-1} at 1500 W kg^{-1}),[50] Co-MOF//AC (24.4 W h kg^{-1} at 429 W kg^{-1}),[51] MOF-derived hierarchical porous carbon film (9.1 W h kg^{-1} at 3500 W kg^{-1}),[52] NiCo-LDH/Zn_2SnO_4//AC (27.3 W h kg^{-1} at 248.3 W kg^{-1}).[53]

With the development of flexible electronic, flexible energy storage devices had attracted more and more attention, so we also assembled AFSCs and tested their electrochemical performance. As shown in Fig. 7(a), no polarization was observed in the CV curve from 1.0 to 1.8 V, showing the satisfactory capacitance behavior.[54,55] In Fig. 7(b), the shape of the CV curve slightly changes at the scan rate from 10 to 100 mV s^{-1}, and it exhibited a typical hybrid capacitance behavior.[56] In Fig. 7(c), the AFSC had a maximum specific capacitance of 45.3 F g^{-1} at 1 A g^{-1}, and its maximum energy density was 20.4 W h kg^{-1} at the power density is 901.5 W kg^{-1}. In Fig. 7(d), the AFSC had almost no change in the shape of the CV curves bent at 90° and 180°, showing excellent electrochemical performance under different bending conditions.[57,58] In order to further test the performance of the AFSC, we tested the capacitance retention of the AFSC after 200 repeated bends. As shown in Fig. 7(e), the retention rate of the AFSC was 79% after 100 repeated bending, showing a good capacitance retention rate. Besides, the capacitance retention remained 64.4% after 200 repeated bending, which could be attributed to the increase in electronic interface transfer resistance of the AFSC after repeated bending.[18,59] In Fig. 7(f), the R_{ct} after bending was much larger than the R_{ct} before bending, indicating the ion diffusion resistance of the AFSC became larger after bending, which was consistent with the capacitance decrease after repeated bending.[60] Furthermore, two series connected AFSCs lit up 10 parallel red LED lights. The above results illustrated that the AFSC had good electrochemical performance under bending and practical value.

4. Conclusion

In summary, we reported a facile hydrothermal method to synthesize flower-like NiCo MOF. The results of XRD and XPS indicated that there were a high crystallinity nickel and cobalt terephthalate framework in NiCo MOF-2. The SEM images showed that the concentration of NaOH had a great influence on the formation and stacking pattern of the nanosheets in NiCo MOF samples. Among NiCo MOF samples, NiCo MOF-2 exhibited extraordinary specific capacitance (927.1 F g^{-1} at 1 A g^{-1}) and the specific capacitance retention reached 69.6% at the current density range of 1.0 to 10 A g^{-1}. This may be attributed to the flower-like structure with a large specific surface area and great electrical conductivity, which was confirmed by BET measurement. With NiCo MOF-2 as the positive electrode and AC as the negative electrode, the NiCo MOF-2//AC hybrid device exhibited maximum energy density of 28.5 W h kg^{-1} at a power density of 400.5 W kg^{-1} and an excellent cyclic stability, which retained 95.4% of the capacitance after 5000 GCD cycles. Furthermore, the AFSC delivered an impressive energy density of 20.4 W h kg^{-1} at the power density of 901.5 W kg^{-1}, and an excellent electrochemical performance under bending (79% after 100 bends and 64.4% after 200 bends). Finally, its energy storage ability for practical application had also been examined by successfully powering ten commercial red LED powerfully. These results indicated that the rapidly synthesized NiCo MOF had great potential as an electrode material for flexible supercapacitors.

Conflicts of interest

There are no conflicts to declare.

Acknowledgements

This work was supported by Research Fund of Guangdong–Hong Kong–Macao Joint Laboratory for Intelligent Micro–Nano Optoelectronic Technology (No. 2020B1212030010), Guangdong Provincial Key Laboratory of Semiconductor Micro Display (2020B121202003), Youth project of Guangdong Foshan joint fund of Guangdong Natural Science Foundation (Grant No. 2020A1515110601, 2019A1515110002).

References

1 M. Inagaki, H. Konno and O. Tanaike, *J. Power Sources*, 2010, **195**, 7880–7903.
2 L. L. Zhang and X. S. Zhao, *Chem. Soc. Rev.*, 2009, **38**, 2520–2531.
3 Z. Wang, Z. Zhu, J. Qiu and S. Yang, *J. Mater. Chem. C*, 2014, **2**, 1331.
4 U. M. Patil, K. V. Gurav, V. J. Fulari, C. D. Lokhande and O. S. Joo, *J. Power Sources*, 2009, **188**, 338–342.
5 Y. Du, P. Xiao, J. Yuan and J. Chen, *Coatings*, 2020, **10**, 892.
6 H. Zheng, T. Zhai, M. Yu, S. Xie, C. Liang, W. Zhao and X. Lu, *J. Mater. Chem. C*, 2013, **1**, 225–229.
7 P. Yang and W. Mai, *Nano Energy*, 2014, **8**, 274–290.
8 Y. Shao, H. Wang, Q. Zhang and Y. Li, *J. Mater. Chem. C*, 2013, **1**, 1245–1251.
9 F. Saleki, A. Mohammadi, S. E. Moosavifard, A. Hafizi and M. R. Rahimpour, *J. Colloid Interface Sci.*, 2019, **556**, 83–91.
10 X. Zhang, X. Liu, R. Yan, J. Yang, Y. Liu and S. Dong, *J. Mater. Chem. C*, 2020, **8**, 2008–2013.
11 C. Zhu, T. Liu, F. Qian, T. Y. Han, E. B. Duoss, J. D. Kuntz and Y. Li, *Nano Lett.*, 2016, **16**, 3448–3456.
12 X. Shi, S. Zheng, Z. Wu and X. Bao, *J. Energy Chem.*, 2018, **27**, 25–42.
13 C. C. Xiong, B. Li, X. Lin, H. Liu, Y. Xu, J. Mao, T. Li and Y. Ni, *Composites, Part B*, 2019, **165**, 10–46.

© 2022 The Author(s). Published by the Royal Society of Chemistry

Open Access Article. Published on 16 February 2022. Downloaded on 12/9/2025 1:56:21 AM.
This article is licensed under a Creative Commons Attribution-NonCommercial 3.0 Unported Licence.

14 T. Le, D. Aradilla, G. Bidan, F. Billon, M. Delaunay, J. M. Gérard and O. Sel, *Electrochem. Commun.*, 2018, **93**, 5–9.
15 Y. Ma, M. Wang, N. Kim, J. Suhr and H. Chae, *J. Mater. Chem. A*, 2015, **3**, 21875–21881.
16 C. Tan and H. Zhang, *Chem. Soc. Rev.*, 2015, **44**, 2713–2731.
17 Y. Shao, J. Li, Y. Li, H. Wang, Q. Zhang and R. B. Kaner, *Mater. Horiz.*, 2017, **4**, 1145–1150.
18 Y. Bai, R. Liu, E. Li, X. Li, Y. Liu and G. Yuan, *J. Alloys Compd.*, 2019, **777**, 524–530.
19 H. Jiang, T. Zhao, C. Li and J. Ma, *J. Mater. Chem.*, 2011, **21**, 3818–3823.
20 Y. Peng, Y. Li, Y. Ban, H. Jin, W. Jiao, X. Liu and W. Yang, *Science*, 2014, **346**, 1356–1359.
21 T. Rodenas, I. Luz, G. Prieto, B. Seoane, H. Miro, A. Corma and J. Gascon, *Nat. Mater.*, 2015, **14**, 48–55.
22 M. Eddaoudi, H. Li and O. M. Yaghi, *J. Am. Chem. Soc.*, 2000, **122**, 1391–1397.
23 M. Zhao, Y. Wang, Q. Ma, Y. Huang, X. Zhang, J. Ping, Z. Zhang, Q. Lu, Y. Yu, H. Xu, Y. Zhao and H. Zhang, *Adv. Mater.*, 2015, **27**, 7372–7378.
24 S. Zhao, Y. Wang, J. Dong, C. T. He, H. Yin, P. An and Z. Tang, *Nat. Energy*, 2016, **1**, 1–10.
25 D. Zheng, H. Wen, X. Sun, X. Guan, J. Zhang, W. Tian, H. Feng, H. Wang and Y. Yao, *Chem.–Eur. J.*, 2020, **26**, 17149–17155.
26 L. Liu, Y. Yan, Z. Cai, S. Lin and X. Hu, *Adv. Mater. Interfaces*, 2015, **5**, 1701548.
27 Q. Wang, L. Shao, Z. Ma, J. Xu, Y. Li and C. Wang, *Electrochim. Acta*, 2018, **281**, 582–593.
28 Y. Jiao, G. Chen, D. Chen, J. Pei and Y. Hu, *J. Mater. Chem. A*, 2017, **5**, 23744–23752.
29 Q. Wang, Q. Wang, B. Xu, F. Gao, F. Gao and C. Zhao, *Electrochim. Acta*, 2018, **281**, 69–77.
30 L. Shao, Q. Wang, Z. Ma, Z. Ji, X. Wang, D. Song, Y. Liu and N. Wang, *J. Power Sources*, 2018, **379**, 350–361.
31 C. Ye, Q. Qin, J. Liu, W. Mao, J. Yan, Y. Wang, J. Cui, Q. Zhang, L. Yang and Y. Wu, *J. Mater. Chem. A*, 2019, **7**, 4998–5008.
32 Y. Yan, P. Gu, S. Zheng, M. Zheng, H. Pang and H. Xue, *J. Mater. Chem. A*, 2016, **4**, 19078–19085.
33 F. Xu, N. Chen, Z. Fan and G. Du, *Appl. Surf. Sci.*, 2020, **528**, 146920.
34 X. Cao, Y. Shi, W. Shi, X. Rui, Q. Yan, J. Kong and H. Zhang, *Small*, 2013, **9**, 3433–3438.
35 S. Sheng, W. Liu, K. Zhu, K. Cheng, K. Ye, G. Wang, D. Cao and J. Yan, *J. Colloid Interface Sci.*, 2019, **536**, 235–244.
36 Q. Zhang, Y. Wang, B. Zhang, K. Zhao, P. He and B. Huang, *Carbon*, 2018, **127**, 449–458.
37 Y. Liu, Y. Wang, H. Wang, P. Zhao, H. Hou and L. Guo, *Appl. Surf. Sci.*, 2019, **492**, 455–463.
38 W. Zhao, Y. Zheng, L. Cui, D. Jia, D. Wei, R. Zheng, C. Barrow, W. Yang and J. Liu, *Chem. Eng. J.*, 2019, **371**, 461–469.
39 W. Chu, Y. Hou, J. Liu, X. Bai, Y. F. Gao and Z. Cao, *Electrochim. Acta*, 2020, **364**, 137063.
40 C. Guan, X. Liu, W. Ren, X. Li, C. Cheng and J. Wang, *Adv. Energy Mater.*, 2017, **7**, 1602391.
41 Q. Li, C. Lu, C. Chen, L. Xie, Y. Liu, Y. Li, Q. Kong and H. Wang, *Energy Storage Mater.*, 2017, **8**, 59–67.
42 J. Pu, F. Cui, S. Chu, T. Wang, E. Sheng and Z. Wang, *ACS Sustainable Chem. Eng.*, 2013, **2**, 809–815.
43 S. G. Mohamed, I. Hussain and J. J. Shim, *Nanoscale*, 2018, **10**, 6620–6628.
44 G. Sun, L. Ma, J. Ran, X. Shen and H. Tong, *J. Mater. Chem. A*, 2016, **4**, 9542–9554.
45 M. Li, W. Yang, J. Li, M. Feng, W. Li, H. Li and Y. Yu, *Nanoscale*, 2018, **10**, 2218–2225.
46 G. Liu, B. Wang, T. Liu, L. Wang, H. Luo, T. Gao, F. Wang, A. Liu and D. Wang, *J. Mater. Chem. A*, 2017, **6**, 1822–1831.
47 J. J. Zhou, X. Han, K. Tao, Q. Li, Y. L. Li, C. Chen and L. Han, *Chem. Eng. J.*, 2018, **354**, 875–884.
48 T. Van Ngo, M. Moussa, T. T. Tung, C. Coghlan and D. Losic, *Electrochim. Acta*, 2020, **329**, 135104.
49 J. Gu, L. Sun, Y. Zhang, Q. Zhang, X. Li, H. Si, C. Sun, Y. Gong and Y. Zhang, *Chem. Eng. J.*, 2020, **385**, 123454.
50 T. Deng, Y. Lu, W. Zhang, M. Sui, X. Shi, D. Wang and W. Zheng, *Adv. Energy Mater.*, 2018, **8**, 1702294.
51 R. Ramachandran, C. Zhao, D. Luo, K. Wang and F. Wang, *Electrochim. Acta*, 2018, **267**, 170–180.
52 Y. Liu, G. Li, Y. Guo, Y. Ying and X. Peng, *ACS Appl. Mater. Interfaces*, 2017, **9**, 14043–14050.
53 X. Ge, C. Gu, Z. Yao, J. Sun, X. Wang and J. Tu, *Chem. Eng. J.*, 2018, **338**, 211–217.
54 L. Kang, S. X. Sun, L. B. Kong, J. W. Lang and Y. C. Luo, *Chin. Chem. Lett.*, 2014, **25**, 957–961.
55 Q. Wang, Q. Wang, B. Xu, F. Gao, F. Gao and C. Zhao, *Electrochim. Acta*, 2018, **281**, 69–77.
56 C. Qu, Y. Jiao, B. Zhao, D. Chen, R. Zou, K. S. Walton and M. Liu, *Nano Energy*, 2016, **26**, 66–73.
57 R. Liang, Y. Du, P. Xiao, J. Cheng, S. Yuan, Y. Chen and J. Chen, *Nanomaterials*, 2021, **11**, 1248.
58 D. W. Kim, S. M. Jung and H. Y. Jung, *J. Mater. Chem. A*, 2020, **8**, 532–542.
59 J. Zhang, J. Sun, T. A. Shifa, D. Wang, X. Wu and Y. Cui, *Chem. Eng. J.*, 2019, **372**, 1047–1055.
60 T. Guan, L. Shen and N. Bao, *Ind. Eng. Chem. Res.*, 2019, **58**, 17338–17345.

© 2022 The Author(s). Published by the Royal Society of Chemistry